ADVANCED FUNCTIONAL MATERIALS
www.afm-journal.de

High-Content, Well-Dispersed γ-Fe_2O_3 Nanoparticles Encapsulated in Macroporous Silica with Superior Arsenic Removal Performance

*Jie Yang, Hongwei Zhang, Meihua Yu, Irene Emmanuelawati, Jin Zou, Zhiguo Yuan, and Chengzhong Yu**

Novel composites of iron oxide encapsulated in macroporous silica with excellent arsenic adsorption performance have been successfully developed. Macroporous silica foams with large pore sizes of ≈100 nm and a high pore volume of 1.6 cm^3 g^{-1} are chosen as the porous matrix. Electron tomography technique confirms that γ-Fe_2O_3 nanoparticles with an average particle size of ≈6 nm are spatially well-dispersed and anchored on the pore walls at even a high γ-Fe_2O_3 content of 34.8 wt%, rather than forming aggregates inside the pores or on the external surface. The open large-pore structure, high loading amount, and the non-aggregated nature of γ-Fe_2O_3 nanoparticles lead to increased adsorption sites and thus high adsorption capacities of both As (V) and As (III) without pre-treatment (248 and 320 mg g^{-1}, respectively). Moreover, the composites can reduce the concentration of both As (V) and As (III) from 100 to 2 μg L^{-1}. It is also demonstrated that the composites can be applied in a household drinking water treatment device, which can continuously treat 20 L of wastewater containing As (V) with the effluent concentration lower than the World Health Organization standard.

1. Introduction

Arsenic contamination in natural water is a global threat due to its high toxicity and carcinogenicity.[1–5] Long-term exposure to arsenic-polluted water may result in some negative effects on human health and cause several diseases, such as lungs, bladder, kidneys and skin cancer.[2,4,6] Arsenic in even very low concentrations can still have a strong adverse effect on health, the maximum contaminant level (MCL) of arsenic in drinking water is suggested to be 10 μg L^{-1} instead of the previous limit of 50 μg L^{-1} according to the guideline of World Health Organization (WHO).[7] However, numerous water bodies around the world carry soluble arsenic at concentrations higher than this standard. The arsenic concentration of many ground waters in the western United States is found higher than 10 μg L^{-1},[5] and most tube-wells in South and Southeast Asia do not meet the standard of WHO.[6] To meet the stricter standard of 10 μg L^{-1}, a simple approach for efficient arsenic removal at low concentrations from drinking water is required.

Arsenic mainly exists as arsenite (As (III)) and arsenate (As (V)) in natural water.[8] As (V) is the predominant species under oxidizing conditions and As (III) predominates in moderately reducing environments such as groundwater.[4] Generally, both species are present in water simultaneously. Compared to As (V), As (III) is more toxic and it is generally accepted that it is more difficult to be removed due to its low affinity to various adsorbents.[9,10] To achieve effective As (III) removal, it is required to pre-treat As (III) by oxidizing it to As (V) and/or adjust the pH value before coagulation–precipitation/adsorption processes.[9,11–13] Apparently, the pre-treatment increases the operation cost and causes secondary pollution problems, thus it is disadvantageous for practical applications. It is highly desirable to develop an adsorbent for efficient and cost-effective removal of both As (V) and As (III) without any pre-treatment.

During the past decades, several techniques have been developed in the removal of arsenic from the wastewater, including precipitation followed by solid/liquid separation, adsorption and ion exchange, biological removal processes, and so forth.[2] Due to the low cost, good performance and easy operation, adsorption is considered to be one of the most effective approaches among these technologies. Iron oxide-based materials have been widely used in arsenic removal because of their low cost, natural abundance and effective performance for both As (V) and As (III) removal. However, the adsorption

J. Yang, H. W. Zhang, M. H. Yu, I. Emmanuelawati, Prof. C. Z. Yu
Australian Institute for Bioengineering and Nanotechnology
The University of Queensland
Brisbane, QLD, 4072, Australia
E-mail: c.yu@uq.edu.au
Prof. J. Zou
Materials Engineering and Centre for Microscopy and Microanalysis
The University of Queensland
Brisbane, QLD, 4072, Australia
Prof. Z. G. Yuan
Advanced Water Management Centre
The University of Queensland
Brisbane, QLD, 4072, Australia

DOI: 10.1002/adfm.201302561

performance needs to be further improved. Although some adsorbents, such as Fe_2O_3 CAHNs[14] and γ-Fe_2O_3 CHNs,[15] show the adsorption capacities up to 137.5 mg g^{-1}, only As (V) can be removed. Moreover, whether the arsenic concentration can be reduced to lower than 10 μg L^{-1} is not reported. Other materials such as iron oxide@carbon,[16] cellulose@iron oxide,[17] and Fe_3O_4-RGO[18] can meet the standard of 10 μg L^{-1} suggested by WHO, however their arsenic uptake capacities are relatively low. It is necessary to develop efficient arsenic adsorbents which can simultaneously meet the standard of 10 μg L^{-1} and possess high adsorption capacities for both As (V) and As (III).

Previous studies show that iron oxides (magnetite and maghemite) with sizes of about 12 and 3.8 nm exhibit significantly increased arsenic adsorption capacities compared with iron oxides with large particle sizes, which may result from more adsorption sites being exposed to arsenic species.[19–21] However, nanoparticles tend to aggregate into large particles easily, leading to deteriorated adsorption performance. Besides, it is difficult to practically apply nanoparticles in the wastewater treatment because small particles may cause difficulties in separation and/or diffusion. To avoid these problems, porous materials have been widely used as the matrix to disperse iron oxide to take advantages of small particle size and high surface area, which are important for applications such as adsorption.[16,22–24] Because iron oxide is the active component, well-dispersed iron oxide with a high content in the porous matrix is necessary for the fabrication of arsenic adsorbents with excellent performance. However, at a high content of iron oxide, most studies show aggregated large nanoparticles in the matrix.[23,25,26] Besides, the open pore networks may be blocked by nanoparticles when the nanoparticle size and the pore size are comparable, which affects the mass diffusion and transportation and consequently the effectiveness of adsorption.[16] To overcome these limitations, a careful selection of porous matrix is of utmost importance.[27]

In this work, macroporous siliceous foams (MOSF)[28] with large pores (≈100 nm) and high pore volumes were chosen as the porous matrix to encapsulate iron oxide nanoparticles with a high content. MOSF materials were synthesized via a facile supra-assembly approach using non-ionic block copolymers as supramolecular templates. Previously, MOSF with suitable functionalization have been studied in bio-applications and phosphate adsorption.[29–31] In this study, γ-Fe_2O_3 nanoparticles with an average size of ≈6 nm are spatially well-dispersed on the pore walls of MOSF without blocking the open pore networks even at the highest metal oxide content of 34.8 wt% (**Scheme 1**a). Electron tomography (ET) technique has been used to confirm that dispersed nanoparticles are anchored on the walls rather than aggregates inside the pores or on the external surface. The novel composites show excellent arsenic adsorption performance for both As (V) and As (III) without pre-treatment (Scheme 1b) because of the open pore network, high loading amount and non-aggregated small iron oxide nanoparticles. The uptake capacities of As (V) and As (III) are 248 mg g^{-1} and 320 mg g^{-1}, respectively. Moreover, the composites can reduce the concentration of both As (V) and As (III) from 100 to 2 μg L^{-1}, far below the standard of 10 μg L^{-1} suggested by WHO. The composites were also applied in drinking water treatment, showing promising potential in practical applications for arsenic removal.

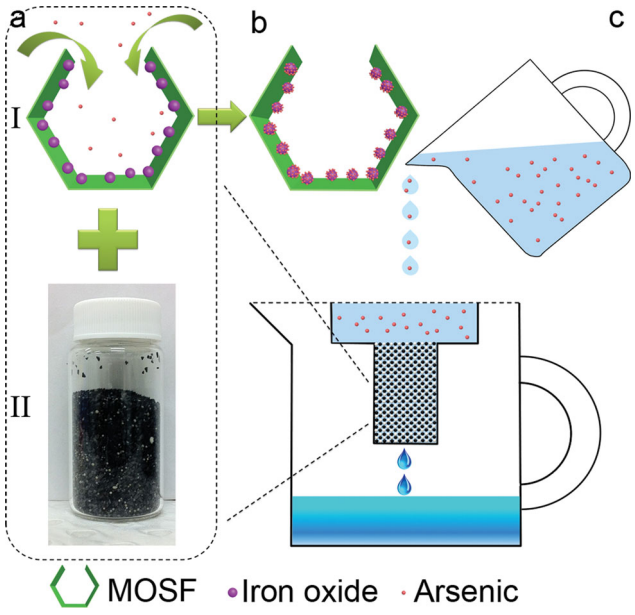

Scheme 1. a) A schematic drawing of γ-Fe_2O_3 nanoparticles encapsulated in MOSF composites (I), and a digital photo of a commercial product (II) used in a household scale drinking water treatment device (Brita). Both materials are used as adsorbents in the filter cartridge in this study. b) A schematic drawing showing that after water purification, arsenic species are adsorbed in the composites. c) The experimental setup for arsenic removal using a jug with a home-made filter cartridge. The pore size of MOSF, the sizes of arsenic anions and iron oxide nanoparticles, and the dimension of the cartridge are not to scale.

2. Results and Discussion

The morphology and structure of MOSF and Fe_XMOSF composites (X = 1, 2, 3, the weight percentage of Fe_2O_3 in the final product is 11.8, 21.0, 34.8%, respectively, see Experimental Section) were investigated by transmission electron microscopy (TEM). MOSF show a foam-like structure packed by polyhedral units following a surface minimization principle (**Figure 1**a).[32] Figure 1b and c are the typical TEM images of Fe_3MOSF at a low and a higher magnification. After the encapsulation of iron oxide nanopaticles, the macroporous foam-like structure of MOSF is well maintained. The distribution of Fe_2O_3 nanoparticles (small dots with a high contrast as shown in Figure 1c) can be clearly observed through the whole sample. The size-distribution histogram of nanoparticles counted in Figure 1c show a broad distribution of particles from 2–13 nm with an average size of ≈6 nm (Figure S1, Supporting Information). A typical high resolution TEM (HRTEM) image of Fe_2O_3 nanoparticle is shown in the inset of Figure 1c, where the (311) lattice fringes of γ-Fe_2O_3 can be clearly observed. To further confirm the successful loading of γ-Fe_2O_3 in MOSF, the dark-field scanning TEM (DF-STEM) technique was employed. In the DF-STEM, the collection of the image is an incoherent process yielding atomic resolution images with strong Z (atomic number)

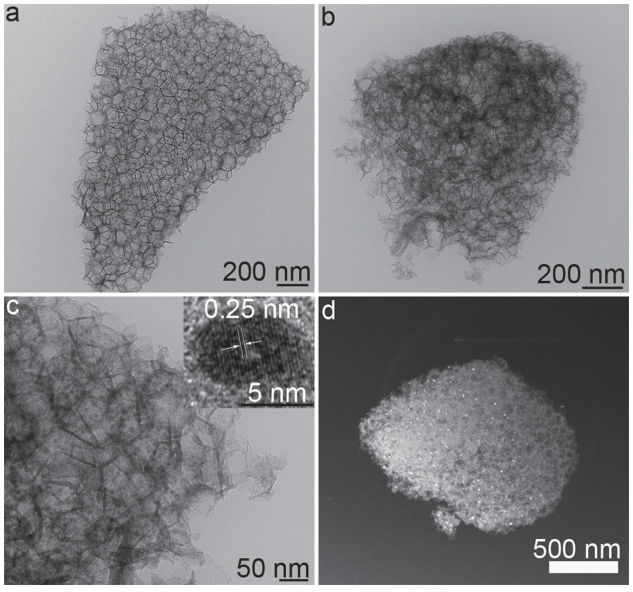

Figure 1. TEM images of a) pristine MOSF, b) Fe_3MOSF at a low magnification and c) a higher magnification. d) DF-STEM image of Fe_3MOSF. Inset of (c) is the HRTEM image of γ-Fe_2O_3 nanoparticles inside the pores of MOSF.

contrast.[33] Thus, heavy atoms such as Fe appear brighter compared to the light atoms (e.g., Si or O). As shown in Figure 1d, a few bright dots can be found in the dark domain of MOSF containing Si and O, indicating the existence of heavy atoms, namely Fe.

Although the presence of nanoparticles in MOSF is confirmed, the distribution of nanoparticles in respect to the pore space is still unknown. Nanoparticles may exist inside the pores or on the external surface. Given inside the pore, nanoparticles may be spatially well-dispersed and attach on the silica wall surface (Scheme S1a, Supporting Information), or exist as aggregates (Scheme S1b, Supporting Information). Because aggregation can decrease the reactivity of nanoparticles,[34] it is important to determine the distribution of γ-Fe_2O_3 inside the composites. However, traditional TEM images are the two-dimensional representation of a three-dimensional object,[35,36] thus it is difficult to differentiate two scenarios (Scheme S1a,b, Supporting Information), but important for applications such as catalysis and separation.[37] To solve this problem, electron tomography (ET), a fast developing technique for the 3D imaging of complex materials,[35] was employed. **Figure 2**a displays the ET slices of Fe_3MOSF in a selected position (yellow cross) viewed from three orthogonal directions (*xy, xz, yz*). If the aggregation of γ-Fe_2O_3 nanoparticles occurs, it should be observed from at least one direction. However, only separated and well-dispersed dark dots can be seen from *xy*, *xz*, and *yz* directions (indicated by black arrows in Figure 2a), indicating that γ-Fe_2O_3 nanoparticles mainly attach on the silica wall surface without aggregation. Besides, the large pore structure of MOSF is still retained at the highest metal oxide content, beneficial for the diffusion of arsenic species into the pores at a high flux.

The restructured 3D structures of three individual pores with polyhedral morphology[32] containing γ-Fe_2O_3 (the area highlighted in Figure 2a) are also shown for the direct visualization (Figure 2b). For clear visualization, the 3D reconstruction was performed by selecting nanoparticles with relatively large particle sizes. Most of the γ-Fe_2O_3 nanoparticles (represented by the red colour) are anchored on the pore walls (represented by the blue, yellow and green colors) as well-dispersed state (similar to the case shown in Scheme S1a, Supporting Information), rather than forming aggregates inside the pores (the case illustrated in Scheme S1b, Supporting Information), leading to the increased active sites. The tomographic reconstructed structures of a local area in the blue polyhedron viewed from different directions are also displayed (Figure 2c–e). The

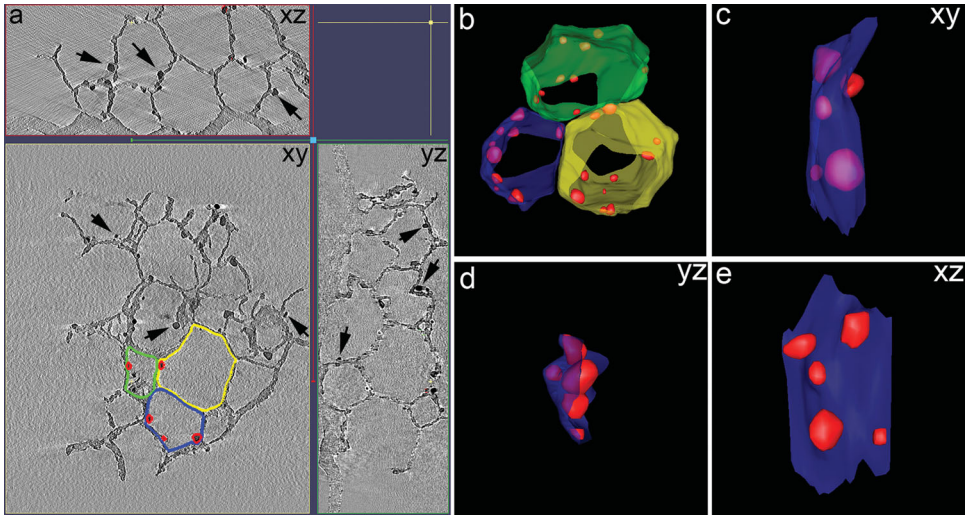

Figure 2. a) ET slices viewed from three orthogonal directions (*xz, xy, yz*). b) Reconstructed 3D structure of three separated pores containing γ-Fe_2O_3 nanoparticles. Images (c–e) are the reconstructed 3D structure of a local area in the blue pore viewed from *xy*, *yz*, and xz directions. Green, blue and yellow represent three individual polyhedrons and red stands for γ-Fe_2O_3 nanoparticles.

attachment of γ-Fe_2O_3 nanoparticles on the silica wall surface can be directly visualized from the models viewed from *xy* and *yz* directions. It is noted that the information provided by these two models (Figure 2c,d) is similar to that of traditional TEM due to the thickness effect, thus difficult to tell whether nanoparticles are aggregated or not. Only the image viewed from *xz* direction can minimize the thickness effect and provides the direct evidence to show that γ-Fe_2O_3 nanoparticles are well-dispersed in one individual pore.

Fe_XMOSF composites with lower iron oxide loading amount (Fe_1MOSF and Fe_2MOSF) were also characterized by TEM. γ-Fe_2O_3 nanoparticles are also found in MOSF with the open pore network, but the number of particles is less compared to Fe_3MOSF due to the lower content of iron oxide (Figure S2a–d, Supporting Information). Scanning electron microscopy (SEM) images show that even at the highest iron oxide content of 34.8 wt%, γ-Fe_2O_3 nanoparticles still deposit in the macroporous matrix (Figure S2e–f, Supporting Information), rather than on the external surface as large particles.[16] Energy dispersive X-ray (EDS) analyses of Fe_XMOSF composites demonstrate the presence of the Fe element in MOSF (Figure S3, Supporting Information), and the atomic ratios of Fe to Si for Fe_XMOSF composites are 10.8%, 19.8% and 37.4% ($X = 1$, 2 and 3, respectively), very close to the feed ratio (Table S1). In addition, the presence of C, Na, and S is also detected by EDS. C comes from the carbon coating process before EDS analyses. The atomic percentage of Na and S are 0.25% and 0.18%, respectively, both originated from the trace amount of inorganic salt Na_2SO_4 used in the synthesis of MOSF. Elemental maps of Fe_3MOSF elucidate the uniform distribution of γ-Fe_2O_3 nanoparticles in MOSF at micron scale (**Figure 3**). Fe, Si, and O elements are uniformly distributed and well correlated with the shape of the sample area.

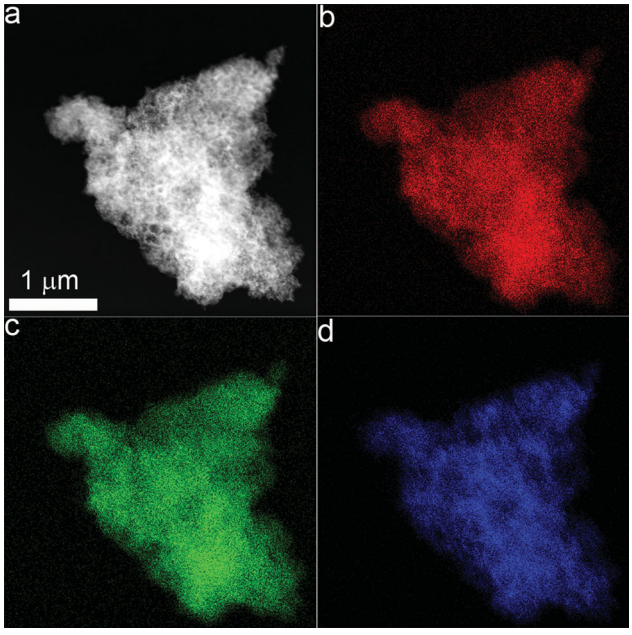

Figure 3. a) HAADF-STEM image and c) the corresponding Si, c) O, and d) Fe elemental maps of Fe_3MOSF.

Fourier transform infrared (FTIR) spectra of MOSF, Fe_3MOSF and two intermediate samples (MOSF-Fe and MOSF-Fe-HAc) are shown in Figure S4, Supporting Information. The spectrum of MOSF (Figure S4a) shows three peaks in 450, 810, and 1065 cm^{-1}, which can be attributed to the rocking, symmetric and asymmetric Si–O–Si stretching.[38,39] Two peaks in 3745 and 970 cm^{-1} can be described as the stretching of isolated silanols[40] and the Si–O in-plane stretching vibrations of the silanol groups,[41] respectively. After encapsulation of iron nitrate, the existence of nitrate anions in MOSF is suggested by two new peaks at 820 and 1398 cm^{-1} (Figure S4b, Supporting Information), which can be assigned to the bending and asymmetric vibrations of nitrate anions.[22] In the following step of exposure to the vapors of acetic acid, the MOSF-Fe-HAc sample with a drastic changed FTIR spectrum (Figure S4c, Supporting Information) can be obtained. The peak appears at 1708 cm^{-1} is due to the asymmetric stretching vibration of carboxyl (-COOH).[42,43] Besides, other four bands at 1585, 1444, 661 and 613 cm^{-1} confirm the formation of trinuclear Fe (III)-acetate complex. To be specific, two strong adsorptions at 1585 and 1444 cm^{-1} are due to the asymmetric and symmetric vibrations of COO^- bridged to Fe (III), and another two bands with relative low intensity are attributed to the OCO and COO deformations, respectively.[44,45] The spectra of Fe_3MOSF and pristine MOSF (Figure S4a,d, Supporting Information) are quite similar due to the silica matrix. The spectrum of Fe_3MOSF also shows the characteristic peaks of H–O–H bending at 1638 and 1554 cm^{-1} due to adsorbed water in sample (Figure S4d, Supporting Information).[46] Although the bands suggesting the formation of Fe–O–Si (around 900 and 680 cm^{-1}) cannot be found in the spectrum of Fe_3MOSF,[47] the absence of the band in 3745 cm^{-1} (Figure S4d, Supporting Information) indicates the disappearance of free silanol groups and γ-Fe_2O_3 nanoparticles are bonded to silica surface by newly formed Si–O–Fe bond.[46] Because the amount of Si–O–Fe bond may be low, thus it cannot be detected by FTIR.

In the range of 680–580 cm^{-1}, a broad band can be clearly seen, corresponding to the Fe–O vibration in magnetite (Fe_3O_4) and maghemite (γ-Fe_2O_3).[22,47] Thus, the formation of iron oxide phase can be clearly indexed. However, it is difficult to distinguish γ-Fe_2O_3 from Fe_3O_4 according to FTIR spectra, thus X-ray diffraction (XRD) and X-ray photoelectron spectroscopy (XPS) measurements were performed. As demonstrated in **Figure 4**, Fe_XMOSF composites with different iron oxide loading amount have the similar diffraction patterns. The broad diffraction peak centered at ≈22° is characteristic for amorphous silica.[48] With the introduction of iron species, the peak of amorphous silica weakens. Apart from the diffraction of silica, several other diffractions (indicated by solid circles) can also be seen and the intensity increases gradually with the increase of iron oxide loading amount from 11.8 to 34.8 wt%. These peaks can be indexed to the diffractions of tetragonal phase γ-Fe_2O_3 (JCPDS Card No. 25–1402) with the cell parameter of a = 8.34 Å and c = 25.02 Å. The relatively broad diffractions also indicate the nanocrystalline nature of γ- Fe_2O_3 in MOSF.

The successful encapsulation of well-dispersed γ-Fe_2O_3 inside MOSF was also confirmed by XPS analysis. The survey spectrum of Fe_3MOSF (**Figure 5**a) shows the presence of Si, O, C, and Fe, in accordance with the results of elemental maps.

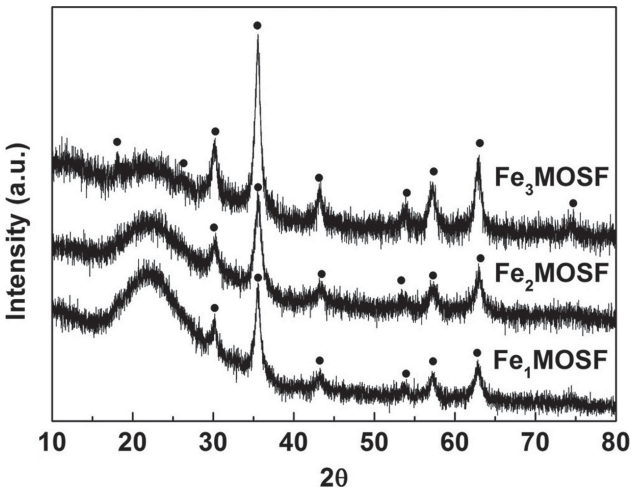

Figure 4. The wide-angle XRD patterns of Fe_xMOSF composites.

Very limited iron content (0.98 wt%) can be found on the outer surface of MOSF (Figure S5, Supporting Information), indicating γ-Fe_2O_3 nanoparticles are almost completely encapsulated in the macropores of MOSF, consistent with ET and SEM characterizations. Two photoelectron peaks located at 711.3 and 724.5 eV are found in the Fe 2p spectrum (Figure 5b), which can be assigned to the Fe $2p_{3/2}$ and Fe $2p_{1/2}$ of γ-Fe_2O_3, respectively.[16] The peak positions of Fe $2p_{3/2}$ and Fe $2p_{1/2}$ for Fe_3O_4 are comparatively lower located at 710.2 and 723.5 eV. Besides, a satellite peak located at 719.0 eV, which is the characteristic peak of γ-Fe_2O_3,[49,50] can also be seen, indicating the well-dispersed iron oxide nanopaticles inside MOSF are γ-Fe_2O_3 rather than Fe_3O_4. The O 1s spectrum (Figure 5c) can be well-fitted to three peaks at 530.4, 532.7, and 533.9 eV, which are attributed to the binding energies of oxygen atoms bonded to Fe, Si, and C, respectively.[51,52] The binding energy of Si 2p is found to be 103.5 eV (Figure 5d), in agreement with the binding energy values of SiO_2 in the previous study.[53]

Nitrogen sorption analyses were carried out for pristine MOSF and Fe_XMOSF composites, and their BET surface areas, pore sizes and total pore volumes are summarized in Table S1, Supporting Information. MOSF and Fe_XMOSF composites show a typical type II adsorption isotherm, relatively large hysteresis loops, and capillary condensation steps at a relatively high pressure ($P/P_0 > 0.9$), indicating the presence of macropores (Figure S6, Supporting Information). Compared with MOSF with the surface area of 448 $m^2\ g^{-1}$ and pore volume of 1.62 $cm^3\ g^{-1}$, a notable reduction in surface area from 250 to 155 $m^2\ g^{-1}$ and pore volume from 1.57 to 0.49 $cm^3\ g^{-1}$ can be clearly observed with the introduction of γ-Fe_2O_3 from 11.8 to 34.8 wt%. It is worth noting that even at a high-content loading of iron oxide (34.8 wt%), Fe_3MOSF composite still possesses an open macroporous structure with a relatively large surface area and high pore volume, which are beneficial for the fast diffusion and transportation of arsenic species.

The formation of non-aggregated small γ-Fe_2O_3 nanoparticles anchored on the pore wall surface is attributed to the homogeneous distribution of iron precursor inside the pores

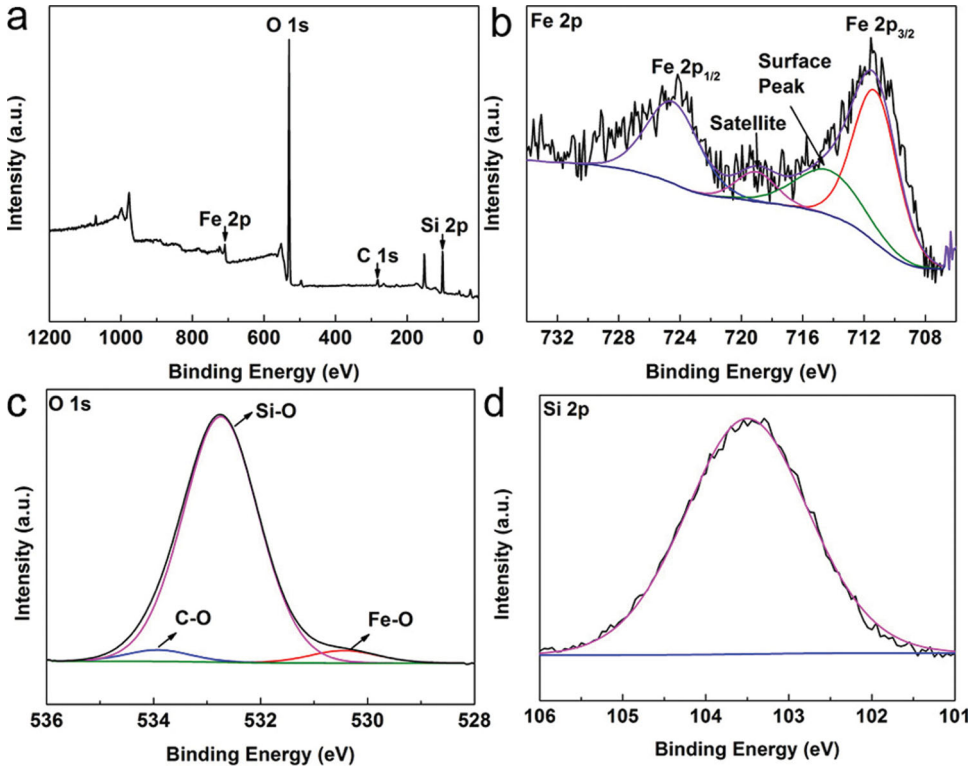

Figure 5. a) XPS survey scan of Fe_3MOSF and the corresponding fine spectra of b) Fe 2p, c) O 1s, and d) Si 2p.

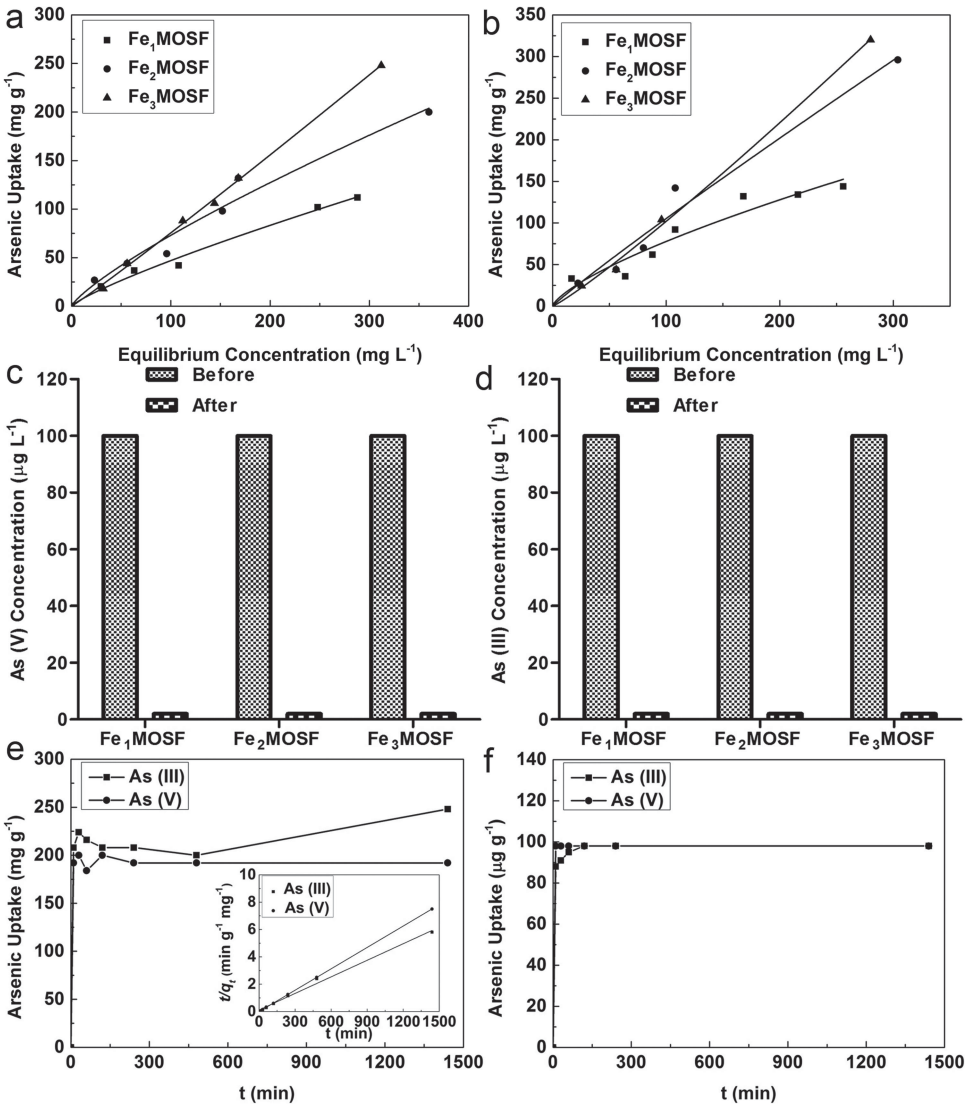

Figure 6. a) As (V) and b) As (III) adsorption isotherms of Fe_xMOSF composites; c) As (V) and d) As (III) adsorption tests of Fe_XMOSF materials with the initial concentration of 100 μg L^{-1}; e,f) Adsorption kinetics of Fe_3MOSF composite in high concentration range of 400 mg L^{-1} and low concentration range of 100 μg L^{-1}, respectively. Inset of (e) is the plot of t/q_t versus t using linear regression.

of MOSF. After impregnation and exposure to vapors of acetic acid, trinuclear Fe (III)-acetate complexes are formed and fixed on the wall surface of MOSF in a homogeneous way as shown in Figure S7, Supporting Information. Calcination at 400 °C causes the thermal decomposition of Fe (III)-acetate complexes and the formation of nuclei of γ-Fe_2O_3. The nucleus of γ-Fe_2O_3 tends to grow into large nanoparticle by consuming surrounding iron precursors. However, the amount of available iron precursors in a local area is limited because of their homogeneous distribution pattern, thus restricting the growth of γ-Fe_2O_3 nanoparticles. Therefore, only non-aggregated small γ-Fe_2O_3 nanoparticles are found anchoring on the silica wall surface of MOSF.

Arsenic adsorption tests were carried out to evaluate the arsenic adsorption capacities of Fe_XMOSF composites. At the initial concentrations of 560 mg L^{-1} for As (V) and 600 mg L^{-1} for As (III), pristine MOSF adsorbs little arsenic with adsorption capacities of 8 mg g^{-1} for As (V) and 16 mg g^{-1} for As (III) (Figure S8, Supporting Information). However, the adsorption capacities can be significantly increased by loading non-aggregated γ-Fe_2O_3 nanoparticles into MOSF. As shown in **Figure 6**a and b, the As (V) and As (III) adsorption can both be well fitted to Freundlich adsorption model according to the high correlation coefficients (R^2, Tables S2,S3, Supporting Information), indicating the adsorption behaviors of As (V) and As (III) on Fe_XMOSF composites can be regarded as a multilayer adsorption process.[14] Fe_XMOSF composites show a significantly increased As (V) adsorption capacities from 112 to 248 mg g^{-1} while iron oxide content varying from 11.8 wt% to 34.8 wt%. Similar results are found in As (III) adsorption. But Fe_XMOSF composites show a better adsorption ability of As (III) than that of As (V). The As (III) adsorption capacities of Fe_XMOSF are

144, 296 and 320 mg g^{-1} (X = 1, 2, and 3, respectively). The adsorption capacities of As (V) and As (III) of Fe_3MOSF are both competitively larger than those of reported arsenic adsorbents (Table S4, Supporting Information). According to the iron oxide content in Fe_3MOSF (34.8 wt%) and considering the contribution of bare MOSF to the adsorption capacities, the adsorption capacities of γ-Fe_2O_3 can be calculated as 675 and 890 mg g^{-1} (Fe_2O_3) for the removal of As (V) and As (III), respectively, about 4–6 times higher than those of nano-sized iron oxides (Table S4, Supporting Information).

The high performance should be attributed to structure of Fe_XMOSF composites: the open large pores facilitate the diffusion and transportation of arsenic; the high-content and well-dispersed iron oxide nanoparticles provide increased active sites for adsorption. XPS was used to confirm the adsorption of As by Fe_XMOSF composites. As shown in Figure S9a (Supporting Information), the survey spectrum of Fe_3MOSF after arsenate adsorption shows the presence of Si, O, C, Fe, and As. The O 1s spectrum (Figure S9b, Supporting Information) presents three peaks with the bonding energies of 529.9, 530.7, and 532.7 eV, which can be assigned to the binding energies of oxygen atoms bonded to As, Fe, and Si, respectively.[17,52,54] The binding energy of As 3d is found to be 44.8 eV (Figure S9c, Supporting Information), indicating the presence of As–O.[17]

Apart from the high adsorption capacities for both As (V) and As (III) in the relatively high concentration range, Fe_XMOSF composites also exhibit an excellent adsorption performance in the low arsenic concentration range. In the natural water bodies, the low to middle arsenic concentration range is ≈100 μg L^{-1}.[55] As shown in Figure 7c,d, with the initial arsenic concentration of 100 μg L^{-1}, the equilibrium concentration of As (V) and As (III) can be both reduced to lower than 2 μg L^{-1} even by Fe_1MOSF with the lowest iron oxide content, suggesting the good arsenic adsorption ability of Fe_XMOSF in the low concentration range.

Because arsenic species distribution is dependent on the pH and redox potential of the natural environment,[2,4,8] the pH value of the water bodies could significantly influence the adsorption performance of arsenic. Therefore, the effect of the initial pH of arsenic solutions on the adsorption capacities was investigated. The experiment was performed with the initial As (III)/As (V) concentration of 100 μg L^{-1} and the contact time of 24 h. The pH value is adjusted between 2 and 10. As shown in Figure S10a (Supporting Information), with raising pH values from 2 to 10, the As (V) uptake capacity keeps constant at 98 μg g^{-1} in the range of 2–6, followed by dropping to 49 μg g^{-1} in pH 10. While the maximum As (III) adsorption capacity of 98 μg g^{-1} is found in pH 6, increasing and decreasing the pH of the solution can both cause the reduction in adsorption capacity. The difference in adsorption capacities as a function the solution pH can be explained by the change of the arsenic speciation and the surface charge of the Fe_3MOSF adsorbent. The point of zero charge (pH_{PZC}) of Fe_3MOSF is measured to be ≈6.1 (Figure S10b, Supporting Information). The surface of Fe_3MOSF is positively charged at pH < pH_{PZC}, and in the pH range of 2–6.1, the predominant species of As (III) and As (V) are H_3AsO_3 with no surface charge and $H_2AsO_4^-$ with negative charge, respectively.[56] Apparently, the electrostatic interaction between positively charged Fe_3MOSF and negatively charged As (V) species is much stronger than that of neutral As (III) species, leading to the better As (V) adsorption performance in the range of 2–6. Besides, the reduction in As (III) adsorption capacity from 98 to 88 μg g^{-1} in the acid range may be due to the partial dissolution of γ-Fe_2O_3 nanoparticles,[57] which results in the reduction in the active sites. In contrast, in the neutral to basic condition of 6–10 (pH > pH_{PZC}), Fe_3MOSF has the negatively charged surface, and the electrostatic repulsions exist between Fe_3MOSF and negatively charged arsenic species ($H_2AsO_3^-$ and $HAsO_4^{2-}$), which are predominant in this pH range. Such repulsions cause the reduction in As (III) and As (V) adsorption capacities in the pH of 6–10.

We also tested the effect of coexisting anions on the arsenic adsorption capacities. As shown in Figure S11, even in the presence of coexisting anions (Cl^-, CO_3^{2-}, SO_4^{2-} and PO_4^{3-}) with an extremely high concentration of 1 g L^{-1}, a negligible decrease in the adsorption capacities of As (III) and As (V) can be seen, indicating the applicability of Fe_XMOSF composite in the capture of arsenic in the practical application.

To further confirm the effectiveness of Fe_XMOSF composite in arsenic removal in water bodies, the adsorption experiments were performed in the real wastewater sample with the initial arsenic concentration of 400 mg L^{-1} since the composition in the real wastewater is more complicated. Although large amounts of other species exist in the wastewater (detailed information is shown in Table S5, Supporting Information), Fe_3MOSF still shows an excellent performance with the adsorption capacities of 200 and 232 mg g^{-1} for As (V) and As (III), respectively, and the reductions in As (III) uptake is only 0.65% (Figure S12, Supporting Information). These results further confirm applicability of Fe_XMOSF composites in arsenic removal from real wastewater without any pre-treatment.

The Fe_XMOSF composite after the adsorption test can be regenerated by stirring with 0.01 mol L^{-1} aqueous sodium hydroxide solution at 25 °C for 4 h. In the second cycle, the adsorption capacities of regenerated Fe_3MOSF are 176 mg g^{-1} for As(V) and 248 mg g^{-1} for As (III) (Figure S13, Supporting Information). The deterioration of the capacity in the second cycle is 29.0% and 22.5% for As (V) and As (III), respectively.

The kinetic studies of As (III) and As (V) were carried out to evaluate the arsenic adsorption rate of Fe_3MOSF with the highest arsenic adsorption capacities in both high and low concentration range, and the fitting results are listed in Tables S2,S3, Supporting Information. The experiment data can be well fitted to pseudo-second order kinetic model (Figure 6e,f), indicating the adsorption process occurs through the chemical interaction.[58] In the high arsenic concentration range of 400 mg L^{-1}, the equilibrium can be reached in the first 30 mins (Figure 6e), suggesting the very fast As (V)/As (III) adsorption rate of Fe_3MOSF in such concentration range. The As (V) adsorption by Fe_3MOSF is ≈10× faster than that of As (III) adsorption as indicated by the rate constants (k, 0.0014 g mg^{-1} min^{-1} vs 0.00015 g mg^{-1} min^{-1}). In the low concentration range of 100 μg L^{-1} (Figure 6f), Fe_3MOSF can rapidly remove 98% of As (V) within 10 min; while only 88% of As (III) is removed by Fe_3MOSF in the first 10 min, and the equilibrium is reached after 2 h with 98% of As (III) being adsorbed. Such results demonstrate that whether in

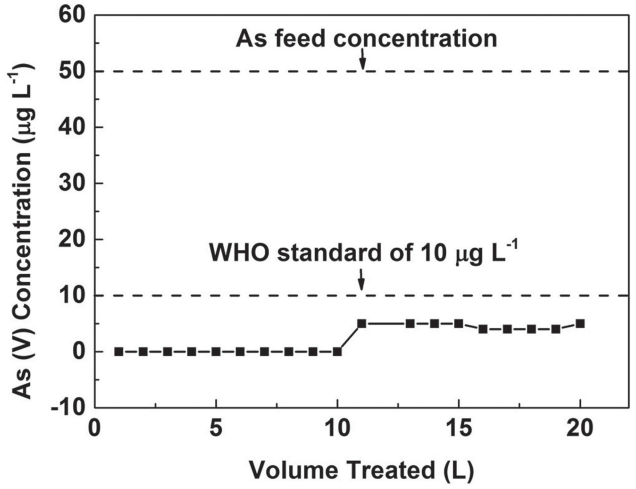

Figure 7. As (V) concentration after passing through the home-made filter cartridge.

high or low concentration range, Fe_3MOSF composite can rapidly remove the arsenic species from wastewater without pre-treatment.

Finally, a jug with a home-made filter cartridge was built as a model device for household drinking water treatment (Scheme 1c). When pouring water into the jug, water will pass through the filter cartridge due to the gravity. For household applications, the high arsenic adsorption capacity is an important parameter considering the long-term use, thus Fe_3MOSF composite was used to fill the filter cartridge. 30 g of a commercially available adsorbent consisting of ion exchange resin and activated carbon for drinking water treatment was also used to assemble the cartridge as a comparison (the digital photo in Scheme 1a). The cartridge filled with the commercial adsorbent can only reduce As (V) content from 50 to 30 μg L^{-1} with 1 L of water poured through the jug. However, by mixing only 0.1 g of Fe_3MOSF composite with 30 g of the commercial adsorbent, 20 L of water containing As (V) can be continuously treated with the outlet concentration less than 10 μg L^{-1} (**Figure 7**), showing its promising application potential in drinking water treatment.

3. Conclusion

In summary, high-content and spatially well-dispersed γ-Fe_2O_3 nanoparticles encapsulated in macroporous silica have been successfully fabricated as the efficient arsenic adsorbents. At a high iron oxide content of 34.8 wt%, ET technique demonstrates that γ-Fe_2O_3 nanoparticles are spatially well-dispersed within the macropores without blocking the open pore network, which gives rise to increased adsorption sites and subsequent high arsenic adsorption capacities. In addition to high uptake performance, both As (III) and As (V) species can be removed without any pre-treatment. Moreover, the residual arsenic concentration can be successfully reduced to 2 μg L^{-1}. The composite also demonstrates excellent performance in household scale drinking water treatment. It is expected that the novel composites have great potential in arsenic removal from polluted water, and can be used in combination with other advanced water treatment methods to meet the stringent limit for water quality control.

4. Experimental Section

Materials: All the chemicals were used as received without further purification. $EO_{20}PO_{70}EO_{20}$ [denoted as P123, where EO is poly-(ethylene oxide) and PO is poly-(propylene oxide)] and $Fe(NO_3)_3{\cdot}9H_2O$ were purchased from Sigma. Tetramethyl orthosilicate (TMOS) and Na_2SO_4 were purchased from Aldrich. Other chemicals were purchased from AJAX chemicals.

Preparation of γ-Fe_2O_3@MOSF: MOSF materials were synthesized at 35 °C in a pH = 5.0 buffer solution in the presence of P123 according to the method reported previously.[28] Briefly, at 35 °C, P123 (1 g) and Na_2SO_4 (1.7 g, 0.40 m) were dissolved in pH = 5.0 NaAc–HAc (Ac = acetate) buffer solution (30 g) (C_t = 0.02 m, where $C_t = C_{NaAc} + C_{HAc}$) to form a homogeneous solution under stirring. To this solution mixture, TMOS (1.52 g) was added under stirring. After 5 minutes, the stirring was stopped. The resultant mixture was kept in a static condition for 24 h and then hydrothermally treated at 100 °C for another 24 h. The white precipitates were filtered, repeatedly washed with water to remove the inorganic salts, and then dried at room temperature. The final MOSF products were obtained by calcination at 550 °C for 5 h.

γ-Fe_2O_3 nanoparticles encapsulated in MOSF composites were synthesized followed a protocol reported by Karakassides and co-workers.[22] Briefly, MOSF (0.2 g) was dispersed in absolute ethanol (5 g), followed by the addition of a 20 wt% ethanolic solution containing $Fe(NO_3)_3{\cdot}9H_2O$. The mixture was stirred at room temperature until the solvents were evaporated. After that, the powder (named as MOSF-Fe) was transferred into a glass bottle which was further placed in an autoclave containing acetic acid (≈20 mL). The autoclave was heated in 80 °C oven for 3 h. After cooling, the solid powder (named as MOSF-Fe-HAc) was dried at 80 °C oven for 15 min to remove any physically absorbed acetic acid. The final γ-Fe_2O_3@MOSF composites were obtained after pyrolysis at 400 °C for 30 min under a 5% H_2–95% Ar atmosphere and at 150 °C for 2 h in air. The weight percentage of Fe_2O_3 in the final products (denoted Fe_XMOSF) was adjusted to be 11.8, 21.0 and 34.8 wt% (X = 1, 2 and 3, respectively) as listed in Table S1, Supporting Information.

Arsenic Adsorption Test: Arsenic adsorption isotherm was acquired through batch experiments. $Na_2HAsO_4{\cdot}7H_2O$ and $NaAsO_2$ were selected as the sources of As (V) and As (III), respectively. The adsorbent (Fe_XMOSF) (0.02 g) was mixed with solution containing different concentration of arsenic (ranging from 0.1 to 560 mg L^{-1} for As (V) and 0.1 to 600 mg L^{-1} for As (III)) (20 mL), followed by shaking (200 rpm) at 25 °C for 24 h to achieve equilibrium. After centrifugation, the arsenic concentration was analysed by the DigiPAsS Digital Portable Arsenic System, Palintest Ltd, England. The limit of detection is 2 μg L^{-1}.

All adsorption isotherm data were fitted with the Freundlich isotherm model. The Freundlich isotherm is expressed as follow:

$$q_{eq} = k C_{eq}^{1/n} \quad (1)$$

where k (mmol$^{(1-n)}$ L^n g^{-1}) is the Freundlich constant that relates to the adsorption capacity, and n is the index that stands for adsorption strength, respectively.

The adsorption kinetic experiments were performed by mixing Fe_XMOSF (0.02 g) with 20 mL of solution containing an initial As concentration of 400 mg L^{-1} or 100 μg L^{-1}. The contact time (t) is calculated after the addition of adsorbent into the solution. The suspension was placed in a rotary shaker with the speed of 200 rpm at 25 °C for 24 h. The suspension was separated by centrifugation at controlled t during the 24 h experiment for arsenic analyses.

The kinetic data of Fe@MOSF were fitted to a pseudo second-order kinetic model, which can be expressed as:

$$\frac{dq_t}{dt} = k\left(q_{eq} - q_t\right)^2 \quad (2)$$

where q_{eq} is the sorption capacity at equilibrium (mg g^{-1}), q_t is the amount adsorbed at a contact time t (mg g^{-1}), and k is the rate constant (g mg^{-1} min^{-1}). Nonlinear least-squares regression analysis was applied to acquire the best estimation of all constants for all the models in arsenic adsorption test.

Sample Characterization: All Fe_XMOSF composites were comprehensively characterized using X-ray diffraction (XRD, Bruker D8 Advanced X-Ray Diffractometer with Ni-filtered Cu Kα radiation at a voltage of 40 mV and a current of 30 mA), scanning electron microscopy (SEM, Philips XL30 operated at 20 kV and JEOL JSM-6460 equipped with energy-dispersive spectroscopy (EDS)), and transmission electron microscopy (TEM, FEI Tecnai F30 operated at 300 kV, and JEOL 2100 operated at 200 kV). The samples for TEM measurements were dispersed in ethanol by ultrasonication for 5 min and then supported onto a holey carbon film on a copper grid. The N_2 adsorption-desorption isotherms were measured at –196 °C on a nitrogen adsorption apparatus (Quadrasorb SI, Quantachrome) after degassing the samples at 180 °C for 6 hours. The Brunauer–Emmett–Teller (BET) surface areas were determined from the adsorption branch of the isotherm in a relative pressure range from 0.05 to 0.30. The pore size distribution (PSD) was determined using Broekhoff and de Boer (BdB) model from the adsorption branch.[59] The pH of the solution was measured by TPS labCHEM-pH meter. X-ray photoelectron spectroscopy (XPS) measurements were performed with a Kratos Axis Ultra X-ray photoelectron spectrometer (Perkin-Elmer). All spectra were acquired at a basic pressure of 2×10^{-7} Torr with Mg Kα excitation at 15 kV. All the results were analysed using the CasaXPS software and corrected by referencing the C 1s peak at 284.8 eV.[60] Fourier transform infrared (FTIR) spectra were collected with ThermoNicolet Nexus 6700 FTIR spectrometer equipped with Diamond ATR (attenuated total reflection) Crystal. For each spectrum, 128 scans were collected at a resolution of 4 cm^{-1} over the range 400–4000 cm^{-1}. Electron tomography was performed using a FEI Tecnai F30 electron microscope operating at 300 kV. All TEM images were recorded at a given defocus in a bright-field mode to show the thickness contrast. The ET specimens were prepared by dispersing the powder samples in ethanol by ultrasonication for 5 min and then depositing them directly onto copper grids (2000 × 1000 slot, Proscitech) with Formvar supporting films. Colloidal gold particles (10 nm) were deposited on both surfaces of the grid as fiducial markers for the subsequent image alignment procedures. The tomographic tilt series were carried out by tilting the specimen inside the microscope around a single axis from 73° to –73° at an increment of 1° under the electron beam. Data processing was carried out by IMOD software.[61]

Supporting Information

Supporting Information is available from the Wiley Online Library or from the author.

Acknowledgements

The authors thank the Australian Research Council for financial support. The authors acknowledge the Australian National Fabrication Facility and Australian Microscopy & Microanalysis Research Facility at the Centre for Microscopy and Microanalysis, The University of Queensland. The authors thank Mr. Qilin Wang from the Advanced Water Management Centre in the University of Queensland for the supply of wastewater.

Received: July 30, 2013
Revised: September 2, 2013
Published online: October 1, 2013

[1] I. Ali, *Chem. Rev.* **2012**, *112*, 5073.
[2] T. S. Y. Choong, T. G. Chuah, Y. Robiah, F. L. G. Koay, I. Azni, *Desalination* **2007**, *217*, 139.
[3] B. K. Mandal, K. T. Suzuki, *Talanta* **2002**, *58*, 201.
[4] D. Mohan, C. U. Pittman, *J. Hazard Mater.* **2007**, *142*, 1.
[5] D. K. Nordstrom, *Science* **2002**, *296*, 2143.
[6] S. Fendorf, H. A. Michael, A. van Geen, *Science* **2010**, *328*, 1123.
[7] WHO, *Guidelines for Drinking Water Quality* **2011**.
[8] W. R. Cullen, K. J. Reimer, *Chem. Rev.* **1989**, *89*, 713.
[9] M. Bissen, F. H. Frimmel, *Acta Hydrochim. Hydrobiol.* **2003**, *31*, 97.
[10] J. F. Ferguson, J. Gavis, *Water Res.* **1972**, *6*, 1259.
[11] M. J. Scott, J. J. Morgan, *Environ. Sci. Technol.* **1995**, *29*, 1898.
[12] M. Zaw, M. T. Emett, *Toxicol. Lett.* **2002**, *133*, 113.
[13] G. S. Zhang, J. H. Qu, H. J. Liu, R. P. Liu, G. T. Li, *Environ. Sci. Technol.* **2007**, *41*, 4613.
[14] F. Z. Mou, J. G. Guan, Z. D. Xiao, Z. G. Sun, W. D. Shi, X. A. Fan, *J. Mater. Chem.* **2011**, *21*, 5414.
[15] F. Z. Mou, J. G. Guan, H. R. Ma, L. L. Xu, W. D. Shi, *ACS Appl. Mater. Interfaces* **2012**, *4*, 3987.
[16] Z. X. Wu, W. Li, P. A. Webley, D. Y. Zhao, *Adv. Mater.* **2012**, *24*, 485.
[17] X. L. Yu, S. R. Tong, M. F. Ge, J. C. Zuo, C. Y. Cao, W. G. Song, *J. Mater. Chem. A* **2013**, *1*, 959.
[18] V. Chandra, J. Park, Y. Chun, J. W. Lee, I. C. Hwang, K. S. Kim, *ACS Nano* **2010**, *4*, 3979.
[19] T. Tuutijarvi, J. Lu, M. Sillanpaa, G. Chen, *J. Hazard Mater.* **2009**, *166*, 1415.
[20] C. T. Yavuz, J. T. Mayo, W. W. Yu, A. Prakash, J. C. Falkner, S. Yean, L. L. Cong, H. J. Shipley, A. Kan, M. Tomson, D. Natelson, V. L. Colvin, *Science* **2006**, *314*, 964.
[21] S. Yean, L. Cong, C. T. Yavuz, J. T. Mayo, W. W. Yu, A. T. Kan, V. L. Colvin, M. B. Tomson, *J. Mater. Res.* **2005**, *20*, 3255.
[22] M. Baikousi, A. B. Bourlinos, A. Douvalis, T. Bakas, D. F. Anagnostopoulos, J. Tucek, K. Safarova, R. Zboril, M. A. Karakassides, *Langmuir* **2012**, *28*, 3918.
[23] X. P. Dong, H. R. Chen, W. R. Zhao, X. Li, J. L. Shi, *Chem. Mater.* **2007**, *19*, 3484.
[24] A. H. Lu, J. J. Nitz, M. Comotti, C. Weidenthaler, K. Schlichte, C. W. Lehmann, O. Terasaki, F. Schuth, *J. Am. Chem. Soc.* **2010**, *132*, 14152.
[25] Y. H. Deng, Y. Cai, Z. K. Sun, D. Gu, J. Wei, W. Li, X. H. Guo, J. P. Yang, D. Y. Zhao, *Adv. Funct. Mater.* **2010**, *20*, 3658.
[26] Y. P. Zhai, Y. Q. Dou, X. X. Liu, B. Tu, D. Y. Zhao, *J. Mater. Chem.* **2009**, *19*, 3292.
[27] Z. X. Wu, D. Y. Zhao, *Chem. Commun.* **2011**, *47*, 3332.
[28] H. N. Wang, X. F. Zhou, M. H. Yu, Y. H. Wang, L. Han, J. Zhang, P. Yuan, G. Auchterlonie, J. Zou, C. Z. Yu, *J. Am. Chem. Soc.* **2006**, *128*, 15992.
[29] K. Qian, J. J. Wan, F. Liu, H. H. Girault, B. H. Liu, C. Z. Yu, *ACS Nano* **2009**, *3*, 3656.
[30] J. J. Wan, K. Qian, L. Qiao, Y. H. Wang, J. L. Kong, P. Y. Yang, B. H. Liu, C. Z. Yu, *Eur. J. Chem.* **2009**, *15*, 2504.
[31] J. Yang, P. Yuan, H. Y. Chen, J. Zou, Z. G. Yuan, C. Z. Yu, *J. Mater. Chem.* **2012**, *22*, 9983.
[32] P. Yuan, X. F. Zhou, H. N. Wang, N. A. Liu, Y. F. Hu, G. J. Auchterlonie, J. Drennan, X. D. Yao, G. Q. Lu, J. Zou, C. Z. Yu, *Small* **2009**, *5*, 377.
[33] S. J. Pennycook, D. E. Jesson, A. J. McGibbon, P. D. Nellist, *J. Electron. Microsc.* **1996**, *45*, 36.
[34] E. M. Hotze, T. Phenrat, G. V. Lowry, *J. Environ. Qual.* **2010**, *39*, 1909.
[35] H. Friedrich, P. E. de Jongh, A. J. Verkleij, K. P. de Jong, *Chem. Rev.* **2009**, *109*, 1613.
[36] P. A. Midgley, R. E. Dunin-Borkowski, *Nat. Mater.* **2009**, *8*, 271.

[37] V. Matsura, Y. Guari, J. Larionova, C. Guerin, A. Caneschi, C. Sangregorio, E. Lancelle-Beltran, A. Mehdi, R. J. P. Corriu, *J. Mater. Chem.* **2004**, *14*, 3026.
[38] M. Prassas, J. Phalippou, L. L. Hench, J. Zarzycki, *J. Non-Cryst. Solids* **1982**, *48*, 79.
[39] J. Y. Ying, J. B. Benziger, A. Navrotsky, *J. Am. Ceram. Soc.* **1993**, *76*, 2571.
[40] S. Jambhrunkar, M. Yu, J. Yang, J. Zhang, A. Shrotri, L. Endo-Munoz, J. Moreau, G. Lu, C. Yu, *J. Am. Chem. Soc.* **2013**, *135*, 8444.
[41] R. Al-Oweini, H. Ei-Rassy, *J. Mol. Struct.* **2009**, *919*, 140.
[42] J. Kathi, K. Y. Rhee, *J. Mater. Sci.* **2008**, *43*, 33.
[43] J. Roggenbuck, T. Waitz, M. Tiemann, *Microporous Mesoporous Mater.* **2008**, *113*, 575.
[44] A. B. Bourlinos, M. A. Karakassides, A. Simopoulos, D. Petridis, *Chem. Mater.* **2000**, *12*, 2640.
[45] K. Nakamoto, in *Infrared and Raman Spectra of Inorganic and Coordination Compounds*, John Wiley & Sons, Inc., **2008**, 149.
[46] C. W. Jung, *Magn. Reson. Imaging* **1995**, *13*, 675.
[47] C. Chaneac, E. Tronc, J. P. Jolivet, *J. Mater. Chem.* **1996**, *6*, 1905.
[48] H. G. Zhu, B. Lee, S. Dai, S. H. Overbury, *Langmuir* **2003**, *19*, 3974.
[49] J. Lu, X. L. Jiao, D. R. Chen, W. Li, *J. Phys. Chem. C* **2009**, *113*, 4012.
[50] X. W. Teng, D. Black, N. J. Watkins, Y. L. Gao, H. Yang, *Nano Lett.* **2003**, *3*, 261.
[51] R. P. Netterfield, P. J. Martin, C. G. Pacey, W. G. Sainty, D. R. Mckenzie, G. Auchterlonie, *J. Appl. Phys.* **1989**, *66*, 1805.
[52] C. D. Wagner, D. A. Zatko, R. H. Raymond, *Anal. Chem.* **1980**, *52*, 1445.
[53] S. S. Chao, Y. Takagi, G. Lucovsky, P. Pai, R. C. Custer, J. E. Tyler, J. E. Keem, *Appl. Surf. Sci.* **1986**, *26*, 575.
[54] M. L. Miller, R. W. Linton, *Anal. Chem.* **1985**, *57*, 2314.
[55] M. Amini, K. C. Abbaspour, M. Berg, L. Winkel, S. J. Hug, E. Hoehn, H. Yang, C. A. Johnson, *Environ. Sci. Technol.* **2008**, *42*, 3669.
[56] P. L. Smedley, D. G. Kinniburgh, *Appl. Geochem.* **2002**, *17*, 517.
[57] B. An, Q. Q. Liang, D. Y. Zhao, *Water Res.* **2011**, *45*, 1961.
[58] Y. S. Ho, G. McKay, *Water Res.* **2000**, *34*, 735.
[59] W. W. Lukens, P. Schmidt-Winkel, D. Y. Zhao, J. L. Feng, G. D. Stucky, *Langmuir* **1999**, *15*, 5403.
[60] E. M. E. Kristensen, F. Nederberg, H. Rensmo, T. Bowden, J. Hilborn, H. Siegbahn, *Langmuir* **2006**, *22*, 9651.
[61] J. R. Kremer, D. N. Mastronarde, J. R. McIntosh, *J. Struct. Biol.* **1996**, *116*, 71.